Measurement report: Temporal variability of vertical profiles of CO_2 and CH_4 over urban environment

Miroslaw Zimnoch[1,*], Michał Gałkowski[3,1,*], Piotr Sekula[2,1,*], Łukasz Chmura[1,2], Jakub Bartyzel[1], Alina Jasek-Kaminska[1,2], Alicja Skiba[1], Jaroslaw Necki[1], Przemyslaw Wachniew[1], and Pawel Jagoda[1]

[1]AGH University of Krakow, Faculty of Physics and Applied Computer Science, Krakow, Poland
[2]Institute of Meteorology and Water Management — National Research Institute, Warsaw, Poland
[3]Max Planck Institute for Biogeochemistry, Department of Biogeochemical Signals, Jena, Germany
[*]These authors contributed equally to this work.

Correspondence: Miroslaw Zimnoch (zimnoch@agh.edu.pl)

Abstract. Understanding the boundary layer dynamics over urban areas is important to improve estimates of the emissions of greenhouse gases (GHG), and predict their atmospheric mole fractions in these areas. Here we present the results of the annual vertical profiling measurement campaign performed in Krakow (Southern Poland). The campaign consisted of 12 monthly-based diurnal measurements of CO_2 and CH_4 molar fraction vertical profiles supplemented by meteorological parameters focused on the investigation of the dynamics of nocturnal boundary layer vertical structure within the urban boundary layer. The profile data were collected using two platforms: (i) a tethered touristic balloon operating commercially in the city centre up to 280 m a.g.l. and (ii) a drone system operating up to 100 m a.g.l., with the selection of the platform based on operational availability and meteorological conditions. CO_2 and CH_4 molar fractions were measured using Picarro G2311-f (Picarro Inc., Santa Clara, California, USA) cavity ring-down spectrometer, while the meteorological conditions along the profile were measured using a set of temperature, relative humidity, pressure and wind low-cost sensors dedicated for application on-board of UAV platforms. The obtained results allowed us to analyse in-depth the formation, development and disappearance of the nocturnal boundary layer. In selected profiles, a CO_2 and CH_4 plumes located over the inversion layer (150-250 m AGL) were detected during the nighttime and morning hours. The application of high-resolution numerical simulations using the WRF-GHG model made it possible to identify the source of CO_2 plume as a power plant located ca. 10 km southwest of the balloon launch location.

1 Introduction

Stabilising the global temperature rise in the XXI century well below 2 °C, and toward 1.5 °C, requires comprehensive mitigation efforts targeting all greenhouse gases (GHG), including both CO_2 and non-CO_2 GHG emissions (Ou et al., 2021). Efforts towards carbon dioxide (CO_2) mitigation are of particular interest to minimise long-term temperature increase, and the peak global warming is proportional to the cumulative CO_2 emissions. Near-term climate forcers which include methane, ozone and atmospheric aerosols have much shorter lifetimes than CO_2, which provides an opportunity for short-term mitigation. Methane (CH_4) is a potent GHG, which has a significantly shorter lifetime compared to CO_2 (total atmospheric lifetime of CH_4 is equal

to 9.1 $\pm$ 0.9 years - IPCC (2021)), mainly due to its reaction with the hydroxyl radical. During 2022, the mole fractions of three greenhouse gases emitted by human activity (CO_2, CH_4 and nitrous oxide), continued their historically high rates of growth in the atmosphere. The global surface average CO_2 mole fraction rose by 2.13 ppm, reaching 417.06 ppm in 2022 (NOAA, 2024). The mole fraction of atmospheric CO_2 is now over 50 % higher than the pre-industrial level of approximately 280 ppm. Background levels of atmospheric methane in 2022 have also increased to an average of 1911.9 ppb. Its annual increase was equal to 14.0 $ppb\,yr^{-}1$, the fourth largest annual increase recorded since NOAA's systematic measurements began in 1983, and followed record growth in 2020 and 2021.

The availability of dense GHG observation networks allows scientists to analyse both long-term trends and anomalies in carbon balance as well as the response of the biosphere to changes in climate observed during the last decades. Knowledge of vertical GHG distribution is crucial for the evaluation of atmospheric models and, when profiles span full troposphere and lower stratosphere also in the calibration and validation of satellite-borne measurements. The low-level GHG profiles contribute indirectly to satellite data validation as well, through improving quality of the atmospheric models. All this components are necessary to improve the ability of atmospheric inversions to resolve emissions at regional and global scale (Keppel-Aleks et al., 2011).

On regional scales, the spatial and temporal distributions of CO_2 and CH_4 in the atmosphere are highly dependent on mesoscale weather systems (Zhang et al., 2022) and the distribution of their large-scale sources and sinks. On sub-regional and local scales, the crucial meteorological variables that determine the GHG variability, like wind speed, wind direction, and the planetary boundary layer (PBL) dynamics are superimposed on highly variable (both in space and time) distribution of sources and sinks of GHGs (van der Woude et al., 2023). The variability in GHGs fluxes to the atmosphere is closely linked to the land-use and land-cover. In urban areas these are highly heterogeneous, and in addition to abundance of human activities responsible for GHGs release, the spatial and temporal distribution of their sources and sinks becomes extremely complex where urban environments are considered. This applies to all GHGs, with the differences remaining in their emission sources: CO_2 sources are road transport, domestic heating, respiration of the inhabitants; methane is being emitted from landfills or artificial wetlands, and SF_6 - from power installations. Through atmospheric transport models, net GHG flux to the atmosphere can be transposed to its mole fraction observed in the local atmosphere. In strong wind conditions, the variability of the local mole fractions of GHGs is dominated by variations in their background values (Thilakan et al., 2022) due to intensive horizontal and vertical mixing of the air. Most of the time however, the local mole fractions are the result of the complex interplay between the sources, sinks, and the structure of atmospheric flows in the PBL. The atmospheric transport occurs not only in horizontal but also vertical directions, and the variability of the turbulence plays a critical role in shaping the vertical distribution of GHGs on diurnal and seasonal scales (Li et al., 2014). It should also be noted that depending on local circumstances, GHGs mole fraction can also be affected by diverse topography (Giovannini et al., 2020), as interactions of the atmospheric dynamics with the orography can significantly influence the transport of the tracers on local or even regional scales. All these factors contribute to increased uncertainty of local dynamics of GHGs, and since the cities are their major sources, to the regional and in consequence the global inventory as well. In this perspective, providing observational data on the urban GHGs becomes crucial to improvement of emissions assessments.

Research on the vertical structure of GHGs has been carried out in the past using multiple methods: stationary point measurements in the profile using the available tall-tower infrastructure (Richardson et al., 2017), tethered balloons (Li et al., 2014), aeroplanes (Fiehn et al., 2020; Gałkowski et al., 2021), unmanned aerial vehicles (UAVs) using different sampling strategies like dedicated compact sensors (Kunz et al., 2018), discrete sampling (Lampert et al., 2020), or aircore systems (Tong et al., 2023) determining the measurements precision and temporal/vertical resolution, or with the use of either ground-based (Dietrich et al., 2021; TCCON, 2023) or spaceborne remote sensing (e.g. TROPOMI, GOSAT, Veefkind et al., 2012; NIES, 2023). The most precise and accurate sources of information on GHG vertical profiles are provided by air samples collected at different altitudes by using aircraft measurement systems (planes, balloons or UAVs), as they can be relatively easily linked directly to WMO scales. They are also, however, usually sparse in space and time due to technical and logistic limitations, including lifting capacity, flight time and maximum reachable altitude. Besides that, they cannot operate during unfavourable weather conditions.

Urban areas, which constitute 2 % of the land surface, are responsible for around 70 % of anthropogenic $\mathrm{CO_2}$ emissions. Transport and buildings are among the largest contributors (Duren and Miller, 2012). A complex topography and land cover within urban areas strongly influence the boundary layer dynamics, being one of the main physical drivers of dispersion processes in near-ground atmosphere. Especially the night-time vertical structure of the Urban Boundary Layer (UBL), as well as the transition phase between stable and convective BL, is crucial for a proper estimation of urban emissions based on a top-down approach using the high-resolution numerical models and ground-based atmospheric observations of GHG (Wei et al., 2020; Bezyk et al., 2023). One of the essential elements in such models is a proper parameterisation of the urban boundary layer (especially during the night time) (Lopez-Coto et al., 2020; Peng et al., 2023). Validation of parameterisation schemes requires observational data containing both meteorological parameters and GHG mole factions in vertical profiles over the urban area. Obtaining such data anywhere poses an organisational and logistical challenge, as measurements of vertical profiles require airborne platforms equipped with heavy instrumentation to achieve the necessary precision and accuracy. In urban areas, the gathering of these data is even more constrained due to legal limitations; therefore, the amount of experiments targeting urban campaigns is relatively limited (e.g. Turnbull et al., 2011; Crawford et al., 2016; Park et al., 2017; Ashworth et al., 2020). Most studies targeting GHG fluxes that include sampling of the atmosphere throughout the vertical extent of the PBL either limit measurements to the areas upwind or downwind of the urban zones (Fiehn et al., 2020), or rely heavily on surface observations of GHGs supplemented by ceilometers and lidars for detection of the mixed layer (Lopez-Coto et al., 2020).

In this work, we report measurements of vertical distributions of the selected GHGs ($\mathrm{CO_2}$, $\mathrm{CH_4}$) within the urban boundary layer of a city of ca. 1 million citizens, together with the description of their diurnal and seasonal variability. Over the course of the selected campaigns, distributions reaching elevations of up to 280 m AGL and 100 m AGL were observed using the balloon and UAV, respectively. An investigation of the source of a detected plume of $\mathrm{CO_2}$ is also performed using a WRF-GHG model support.

2 Methods

2.1 Study area

Krakow is the second largest city in Poland, located in the Little Poland region, with an area of 326.8 km^2 and the number of inhabitants reaching over 800,000 (USK, 2023). The Krakow agglomeration consists of the city itself and the highly populated towns and villages which surround it, together with which the total number of people living in the area is estimated to exceed 1 million. The central part of the city is located in the Wisła (Vistula) River valley, at a mean altitude of about 200 m a.s.l. The valley is oriented along the west-east direction and surrounded by hilly terrain from the south (Western Carpathians region) and relatively flat upland areas from the north (Little Poland Uplands region). The hilltops bordering the city to the north and the south reach about 100 m above the river valley floor, similar to the hilltops in the western part of the valley. The surrounding hills form a semi-concave landform open only to the east, partially sheltering the lowest layers of the atmosphere above the city from the prevailing western winds. A narrow opening immediately to the west (Krakow Gate) creates a passage through which the air can be channelled if the wind conditions are favourable (Figure 1). The local scale processes linked to the impact of relief include frequent air temperature inversions, cold air pool formation, air masses separation at the valley top (valley depth is equal c.a. 100 m), katabatic flows and much lower wind speed in the valley floor than at the hilltops (Sekuła et al., 2021b, a). These factors favour the accumulation of trace gases emitted by local sources within the boundary layer over the city. Krakow represents a typical urban environment, with several anthropogenic and natural CO_2 sources and sinks, like low emission sources, industry, transport, water reservoirs and city biosphere, including citizens and their pets (Jasek-Kamińska et al., 2020). Anthropogenic emissions of methane are associated mainly with natural gas distribution networks, especially dense and potentially leaking in urban centres and numerous landfills in the region (Zimnoch et al., 2019).

Observations of GHG mole fraction and meteorological parameters profiles were carried out using two types of measurement platforms at two locations within the city: (i) tethered touristic balloon operating commercially close to the historical city centre (50.046°N 19.936°E), ca. 1800 m south from the main market square in the Old Town and (ii) ZFS-HEXA multi-rotor drone platform operating next to the building of the Faculty of Physics and Applied Computer Science (AGH site, 50.067°N 19.913°E), located within the campus of AGH University of Krakow, ca. 1800 m west from main market square in the old town (Figure 1). Auxiliary meteorological parameters were also measured on the roof of the faculty building. The direct distance between measurement sites was 2.9 km. Co-located measurements were impossible due to legal restrictions constraining the possibility of UAV operations at the balloon location.

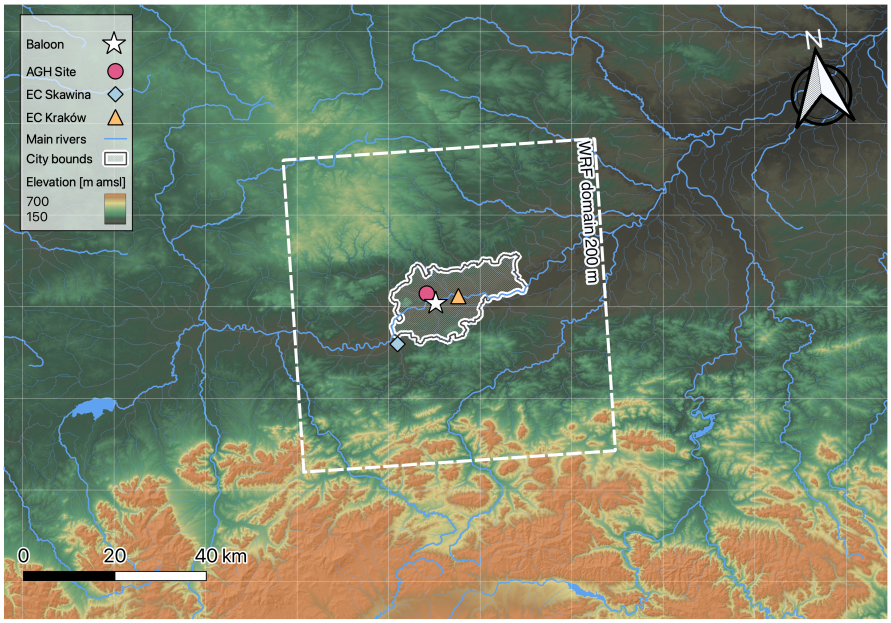

Figure 1. Study area with points of interest overlaid on the topography map.

2.2 Measurements of vertical profiling of GHGs and meteorological parameters

2.2.1 Flight organisation and schedule

Vertical profiles of CO_2 and CH_4 presented in the article were measured with the use of two aircraft platforms - a sightseeing tethered balloon (8 campaigns) and a UAV (3 campaigns). The maximum flight altitude for the drone was equal to 100 m AGL which was determined by the aviation regulations for measurement location. In the case of the balloon, the maximum flight altitude varied between 100 and 280 m AGL, depending on the vertical wind profile and the number of passengers. During working hours, the flight schedule depended on the number of passengers willing to fly (on average every 15 minutes), while during the nighttime hours, flights were made at approximately hourly intervals. Drone flights were performed in hourly intervals during all the campaigns. The timing of the measurement campaign was mostly determined by meteorological conditions. The decision to fly on a given day was first made based on the current weather forecast (IMGW-PIB, 2023) analysed by the flight operator of a drone or sightseeing balloon. The factors precluding flying include the occurrence or forecast wind gusts above 8 $\mathrm{m\,s^{-1}}$ (for UAV wind speed greater than 10 $\mathrm{m\,s^{-1}}$), the risk of storms or the incoming atmospheric front; balloon icing; too low air temperature (for balloon below -10°C); atmospheric precipitation or low visibility. The measurements were performed mostly at night. The balloon's flight vertical speed did not exceed 1 $\mathrm{m\,s^{-1}}$. The flight time depended on the maximum altitude and ranged from 2–3 min (for maximum height equal to 100 m AGL) up to 6–10 min (for maximum height equal to 280 m AGL). For the UAV flights, the speed of the drone also did not exceed 1 $\mathrm{m\,s^{-1}}$, on average it was equal to 0.5 $\mathrm{m\,s^{-1}}$. The flight time for the UAV system varied from 5 to 10 min. Table 1 contains detailed information about each measurement

Table 1. Campaigns details, flight were conducted with the use of two aircraft systems - sightseeing balloon and UAV - at two locations: for balloon (signed as BAL) - 50.046°N 19.936°E, 207 m a.s.l.; for UAV - 50.067°N 19.913°E, 220 m a.s.l.

No.	Date	Sunrise (UTC)	Sunset (UTC)	First flight (UTC)	Last flight (UTC)	Flights number	Platform type
1	10-11.03.2021	05:10	16:30	20:20	07:00	12	BAL
2	28-29.04.2021	05:20	17:50	19:00	08:00	15	BAL
3	01-02.06.2021	02:40	18:40	08:45	05:00	44	BAL
4	13-14.07.2021	02:40	18:50	17:40	06:20	28	BAL
5	07-08.09.2021	04:00	17:10	15:20	08:00	29	BAL
6	11-12.10.2021	04:50	16:00	17:00	07:00	13	UAV
7	25-26.10.2021	05:15	15:30	16:20	10:00	27	BAL
8	24-25.11.2021	06:05	14:50	13:20	12:00	34	BAL
9	22-23.12.2021	06:40	14:40	14:10	11:30	21	BAL
10	11-12.01.2022	06:40	15:00	14:00	05:00	16	UAV
11	31.01-01.02.2022	06:20	15:20	14:00	10:15	19	UAV

campaign including the type of platform and number of performed flights. Campaign characteristics, including flight take-off and histogram of maximum flight altitudes, are presented in Figure S2 in the Supplement.

2.2.2 Observation platforms

At the balloon platform, a set of meteorological sensors was fixed to the outer side of the gondola while the Picarro G2311-f analyser and battery power supply system was placed in the balloon gondola. The air inlet was installed 3 m above the balloon gondola to avoid contamination with $\mathrm{CO_2}$ exhaled by the passengers. In the case of the UAV system, a suite of meteorological sensors consisting of air temperature, relative humidity, atmospheric pressure, and wind speed was installed on top of the drone. In order to minimise the influence of turbulence generated by the propellers and provide proper ventilation of meteorological sensors and air inlet (GHG measurements), they were located in the middle part of a UAV and elevated ca. 25 cm above the propeller height (similar to McKinney et al., 2019; Hedworth et al., 2022). Wind direction measurements were not considered in the current study due to the horizontal oscillations of the balloon and drone during the flight and the strong interference of the electronic compass with the magnetic field generated around the power cables of the drone motors.

To provide detailed information on the location of the measurement, the system was equipped with a GPS receiver and meteorological sensors providing e.g. the altitude estimated with combined GPS and barometer signals. A detailed analysis has shown that the altitude calculated from the barometric formula is more precise than GPS measurements (Equation 1).

$$h = \left[\left(\frac{P}{P_0} \right)^{1/5.257} - 1 \right] \times \frac{T}{0.0065} \tag{1}$$

Where: h - altitude in m AGL; P_0 - atmospheric pressure at the surface level in hPa; P - atmospheric pressure at the current position in hPa; T - air temperature at the current position in K.

Based on the analysis of the obtained data and the literature review, it was assumed that only the measurements collected during the ascent were representative of atmospheric conditions in the vertical profile. In the case of balloon campaigns, during the descending flight, the balloon often began to rotate, which had a significant impact on the measurement of meteorological parameters (visible on wind measurements) and GHGs mole fractions under specific conditions. In the case of the ascending flight, the rotation of the balloon was much less frequent. Furthermore, since the air inlet was located above the balloon gondola, during the descent measured air might be contaminated with the passengers breathing. For UAV-based measurements, recent studies indicated that vertical measurements of gaseous pollutants during the ascent are characterised by the lowest relative error (order of a few %). During the descent of the drone, depending on atmospheric stability conditions, the relative error of measured mole fractions of gaseous pollutants may be even an order of magnitude higher (Hedworth et al., 2022).

2.2.3 Measurements of $\mathbf{CO_2}$ and $\mathbf{CH_4}$ mole fractions

Measurements of carbon dioxide and methane mole fractions presented here were performed by CRDS Picarro G2311-f analyser. For vertical profiling, the instrument operated in the Flux (Low Flow) mode, enabling measurements with a precision of 0.2 ppm for $\mathrm{CO_2}$ and 3 ppb for $\mathrm{CH_4}$ at a frequency of 10 Hz. Before and shortly after each measurement campaign listed in Table 1, a calibration procedure was performed. It involved measuring mole fractions of two standard mixtures of known composition for one hour each. In the course of each campaign, a total of eight standard mixtures were used, ranging from 374 to 521 ppm for $\mathrm{CO_2}$, and from 1880 to 2641 ppb for $\mathrm{CH_4}$. The set of calibration standards consisted of two primary standards provided by the Integrated Carbon Observation System (ICOS) calibration centre and six working standards produced in the greenhouse gas measurement laboratory at AGH University of Krakow. For maintaining the WMO scale the laboratory is participating in a periodic intercomparison excercises. To avoid measurement contamination by human respired $\mathrm{CO_2}$ during the balloon campaigns, a 10 m long 1/8" OD inlet tube was used allowing to place the air inlet ca. 3 m above the balloon gondola. In the case of drone campaigns 200 m long, a 4 mm OD inlet tube was used to connect the air inlet fixed to the UAV with the stationary analyser, located in the laboratory. The Picarro pump was sufficient for flushing the tube. Inlet tubing introduced a signal delay which was determined before each campaign through a breath test injecting $\mathrm{CO_2}$-rich air respired by the operator and measuring the response time of the analyser (Figure S1). The final reported values were obtained by correcting the raw data using the calibration lines ($\mathrm{y} = 1.001\mathrm{x} + 2.7192$ for $\mathrm{CO_2}$ and $\mathrm{y} = 0.996\mathrm{x} + 12.109$ for $\mathrm{CH_4}$) obtained during all available calibration procedures. In the case of both species, the correlation coefficient R^2 for calibration lines was equal to 1 within four significant digits. The maximum long-term drift of measured standards molar fractions was 0.2 ppm for $\mathrm{CO_2}$ and 1 ppb for $\mathrm{CH_4}$, respectively. We applied internal instrument water correction, which is sufficient in the typically observed ranges of water vapour mole fractions (Reum et al., 2019).

2.2.4 Sensors for meteorological parameters

The profiles of meteorological parameters presented in the article were measured using three measurement systems: the AirDust system (designed and constructed in-house at the Environmental Physics Group, AGH University of Krakow), the sonic anemometer TriSonica™ Mini Wind and Weather Sensor (Anemoment LLC, Longmont, CA, USA) and the Mini Weather Station (HY-WDC6SE, HONGYUV, China). The auxiliary stationary measurements are described in the next chapter. The AirDust system and the acoustic wind sensor TriSonica™ were dedicated for measurement with the use of unmanned aerial vehicle (Sekuła et al., 2021c). To provide meteorological sensor redundancy during the balloon campaigns, the Mini Weather Station (HY-WDC6SE) was used. Due to its size and weight as well as the difficulty in mounting it over UAV, it was not used in drone measurements. For balloon measurements, it was possible to use all three systems in parallel thanks to the substantially larger lifting capacity and available space than in the UAV-based system. Due to a number of technical complications, measurements of meteorological parameters in individual sampling campaigns were carried out by different sets of sensors. Detailed information on sensor specifications used in the study is summarised in Table 2. As the individual sensors varied in their sensitivities response times, we have selected the best-performing of the available data for our analysis. Table S1 compares individual meteorological parameters measured by sensors deployed in balloon and UAV-based campaigns. Information on which sensors were used in each campaign is listed in Table S2.

AirDust measurement system

The ultra-light measurement AirDust system was dedicated to meteorological measurements within the urban boundary layer. The system was based on the Arduino MKR ZERO microcontroller, responsible for communication between the sensors and for storage of the measurements on the memory card. The system was powered by a drone battery via a step-down converter reducing the input voltage from 22 V to 5 V at 2 A. Air temperature, relative humidity and atmospheric pressure were measured using a digital sensor (BME280, Bosch Sensortec GmbH, Reutlingen, Germany). To monitor temperature changes within the given vertical profile with a better spatial resolution, the system was also equipped with a thermocouple type T. Since the response time of the T-type thermocouple to temperature changes is shorter than for the BME280 sensor, by default, the measurement was taken from the thermocouple. For the corrections of thermocouple bias error and in the event of technical issues with the thermocouple, the BME280 sensor was used. The sampling frequency of the AirDust system was set to 1 Hz. Technical specification of the AirDust system is presented in Table 2.

TriSonica™ anemometer

The second measurement system used in the measurement campaigns was based on the acoustic anemometer TriSonica™. It was used to monitor horizontal wind components in the studied vertical profile. The system was equipped with an Arduino MKRZERO microcontroller for data storing and the NEO-7 GNSS module (u-blox AG, Thalwil, Switzerland) which allows monitoring of the horizontal and vertical position of the sensors. The TriSonica™ sensor is equipped with a 3D sonic anemometer, temperature, pressure and humidity sensors, as well as a magnetometer and 3D accelerometer for correcting the wind speed and wind direction. The measurements of air temperature, pressure and humidity from the TriSonica sensor were not used in this study due to the fact their inertia was larger than those used in the AirDust system. To avoid measurement

disturbances caused by turbulence generated by the drone's propellers during the UAV-based campaigns, the system was fixed on a small extension arm ca. 30 cm over the drone platform. The anemometer can measure wind speed and wind direction with different sampling frequencies, from 1 Hz to 10 Hz. It was found that measurements with a sampling frequency equal to 1 Hz were characterised by the smallest number of incorrect measurements (glitches). Therefore, the frequency of the system was set to 1 Hz. Analysis of the wind direction observations in the vertical profile revealed that reliable measurements were difficult to achieve. The idea of wind direction correction using an onboard magnetometer during the flight was tested (balloon and UAV-based campaigns). In the case of UAV-based campaigns magnetic field disturbance generated by the currents supplying the drone's motors generated too much noise making it impossible to use a magnetometer for a correction procedure. Finally, wind direction measurements in vertical profiles were excluded from further analysis due to their unreliability. The specification of the TriSonica^{TM} sensor was included in Table 2 (only wind speed measurements).

Mini Weather Station

The Mini Weather Station was used to monitor horizontal wind speed, air temperature, relative humidity and atmospheric pressure in a vertical profile. It is worth mentioning that the inertia of air temperature and relative humidity sensors in the Mini Weather Station is larger than for the sensors used in the AirDust system. Due to this fact, the Mini Weather Station was used as a backup system for AirDust sensors. The Mini Weather Station provides also measurements of atmospheric precipitation and radiation components which were not used in this study. The sampling frequency of the HY-WDC6SE station was equal to 1 Hz. Technical specification of the Mini Weather Station for selected meteorological parameters is presented in Table 2.

Sensors calibration

Calibration of all meteorological sensors was performed through a comparison against the stationary meteorological station operating at the AGH site (see Sections 2.1 and 2.3). Air temperature, relative humidity, atmospheric pressure and wind at the level of 20 m AGL, were measured using a WXT520 (Vaisala, Vantaa, Finland) weather station. Figure S3 presents the comparison between tested sensors and reference instruments over three consecutive days (from 29 April to 2 May 2022) with one-hour resolution, together with linear regression equations for individually tested parameters. The calibration equation and correlation coefficient R^2 obtained with the use of linear regression are presented in Table 3. For calibration of the anemometers, the intersection points of the regression lines were set to 0. Tests of the sensors showed the correct measurement for atmospheric calm, where the wind speed was equal to 0 $\mathrm{m\,s^{-1}}$. For the remaining instruments, the formula $\mathrm{y = Ax + B}$ was used in the calibration. Formulas of linear regression were used to correct the systematic error of measurements presented in this article.

2.3 Auxiliary stationary measurements

In addition to measurements conducted directly at the site of the measurement campaigns, continuous observations of meteorological parameters and $\mathrm{CO_2}$ and $\mathrm{CH_4}$ mole fractions were carried out on the university campus providing data representing the urban boundary layer in the vicinity of the campaigns. Meteorological measurements were conducted using the Vaisala WXT520 weather station located on the roof of the Faculty of Physics and Applied Computer Science building (50.067°N 19.913°E) ca. 20 m AGL The station has been operating at this location since 2012 and provides long-term one-minute tempo-

Table 2. Technical specifications of three meteorological systems.

Bosh BME280 (AirDust system)			
Parameter	Operating range	Accuracy	Resolution
Relative Humidity	0 ÷ 100 %	±3 %	0.008 %
Air Pressure	300 ÷ 1100 hPa	±0.12 hPa	1.8 * 10^{-3} hPa
Temperature	-40 °C ÷ 85°C	±1 °C	0.01 °C
Dimension/Weight	110 × 90 × 50 mm / 0.235 kg		
Thermocouple type T (AirDust system)			
Temperature	-50 °C ÷ 150 °C	±0.1 °C	0.01 °C
TriSonica™ sonic anemometer			
Parameter	Operating range	Accuracy	Resolution
Wind Speed	0 ÷ 50 $\mathrm{m\,s^{-1}}$	±0.1 $\mathrm{m\,s^{-1}}$ (0–10 $\mathrm{m\,s^{-1}}$)	0.1 $\mathrm{m\,s^{-1}}$
Dimension/Weight	91 mm × 91 mm × 52 mm / 0.05 kg		
Mini Weather Station (HY-WDC6SE)			
Parameter	Operating range	Accuracy	Resolution
Wind Speed	0 ÷ 40 $\mathrm{m\,s^{-1}}$	±5 %	0.1 $\mathrm{m\,s^{-1}}$
Relative Humidity	0 ÷ 100 %	±5 %	1 %
Air Pressure	150 ÷ 1100 hPa	±1 hPa	0.1 hPa
Temperature	-40 °C ÷ 80 °C	±0.5 °C	0.1 °C
Dimension/Weight	Φ84 mm × 210 mm / 0.33 kg		

Table 3. Meteorological sensors calibration details. All anemometers were calibrated using the $y = Ax$ formula, for all other instruments $y = Ax + B$ was used.

Sensor ID	Meteorological parameter	R^2	Equation
Meteo WDC6SE	Wind speed	0.95	$y = 0.95x$
	Air temperature	0.99	$y = 1.02x - 0.62$
	Atmospheric pressure	0.99	$y = 1.01x - 7.26$
	Relative humidity	0.99	$y = 1.06x - 3.07$
TriSonica	Wind speed	0.96	$y = 0.85x$
Thermocouple	Air temperature	0.99	$y = 1.02x - 0.89$
BOSH BME280	Air temperature	0.99	$y = 0.98x + 0.73$
BOSH BME281	Atmospheric pressure	0.99	$y = 1.04x - 34.50$
BOSH BME282	Relative humidity	0.99	$y = 0.96x - 1.60$

ral resolution information about the ambient temperature, relative humidity, atmospheric pressure, wind speed, wind direction and precipitation. The meteorological dataset is supplemented by the radiation dataset collected with an NR01 (Hukseflux Thermal Sensors B.V., Delft, The Netherlands) net radiometer installed at the same location ca. 40 m AGL The radiometer consists of two sets of sensors for different wavelength ranges (a pyranometer and a pyrgeometer), one set facing up and another facing down, enabling measurement of all components of net radiation balance. In addition to meteorological measurements, observations of $\mathrm{CO_2}$ and $\mathrm{CH_4}$ molar fractions in the periods between profiling campaigns were also carried out continuously using the same Picarro analyser for profile measurements. The air inlet was placed at the location of the net radiometer (ca. 40 m AGL).

2.4 WRF-GHG model

To support the measurements presented in the study, the Weather Research and Forecast model WRF (Skamarock et al., 2008) utilising the Advanced Research WRF (ARW) core was used with the Greenhouse Gas module (GHG) enabled. WRF-ARW is an Eulerian NWP model developed in a collaboration headed by the National Center for Atmospheric Research (NCAR). It integrates the non-hydrostatic, fully compressible Euler equations in flux form on classic terrain-following or hybrid vertical coordinates. The WRF model has been successfully applied from global- to local scale, with effective downscaling possible through one- or two-way nesting. Here, we operate the system as a limited area model, using meteorological boundary conditions from ERA5 reanalyses (Hersbach et al., 2017), downloaded at 0.25°x 0.25°horizontal and 37 pressure-level vertical resolution. The basic WRF model was augmented by the GHG module from the Chem suite (Grell et al., 2005), allowing for the emission, transport and mixing of inert $\mathrm{CO_2}$ tracers (Beck et al., 2013).

The model was run in a one-way nested configuration with three domains of 5 km, 1 km and 200 m horizontal resolution, respectively. These were run with time steps of 25 s, 5 s and 1 s. The model top was set at a pressure of 50 hPa, corresponding to approximately 20 km a.m.s.l., with 80 full model levels defined using the hybrid vertical coordinate system. As night-time transport of tracers was critical for the current study, we have opted for high resolution of the vertical levels in the lower atmosphere, with the lowest layer thickness set to 25 m and approximately 40 levels below 3 km altitude. For both nested domains, default MODIS land use category maps and elevation maps were replaced by fields interpolated from Corine Land Cover (CLC) valid for the year 2018 (V20u1, CLC, 2020) and Copernicus Digital Elevation Model (DEM; ESA, 2022) providing the most recent version and enough spatial ressolution for the nested domains configuration. Remapping of CLC to MODIS categories was performed following Siewert and Kroszczynski (2020). Additionally, physical soil properties in the innermost domain were augmented by data from the LUCAS database (Ballabio et al., 2016), obtained from European Soil Data Centre (ESDAC, 2023) following the procedure described by Dy and Fung (2016). For our experiment, WRF was configured with the Thompson microphysics scheme, RRTMG schemes for longwave and shortwave radiation revised MM5 scheme for surface layer physics, and NOAH-MP land surface model. Grell 3D cumulus parameterization was enabled in the parent domain only. As all our domains are run in grey-zone horizontal resolutions, we have applied the Shin-Hong PBL scheme in all nests. Momentary model output was saved every 5 minutes. Comparisons to the observational data were done using the output with minimal temporal difference.

Over a subset of the campaigns, distinctly elevated plumes of CO_2 were observed at elevations close to 200 m AGL. To identify a potential emission source responsible for the elevated mole fractions, we have used the WRF-GHG model with two tagged tracers of CO_2 representing emissions from two nearby coal power plants. For each of the sources, we have implemented constant fluxes of CO_2 at a constant rate equal to the annual emission reported in the recent Industrial Emission Reporting database for the year 2020 (EEA, 2023). As the elevated plumes were observed under predominantly stable atmospheric conditions, it was decided to set the source of emission into a single model layer in order to overestimate mixing at the source. Simultaneously, we have partially taken the plume buoyancy into account by selecting the layer at 4/3 of the height of the emitting stack, following the approach used in the classical Gaussian plume methods. While the realistic plume-rise mechanisms have been previously recognised as an important source of model errors where quantification of the emission is attempted (Brunner et al., 2023), it was assessed that more sophisticated plume-rise algorithms were not necessary for our limited purpose of determination of the single industrial point source only.

3 Results and Discussion

3.1 Overview

Stationary measurements of GHGs at AGH site (AGH University of Krakow, Faculty of Physics and Applied Computer Science, 50.067°N 19.913°E) during the period from March 2021 till April 2022 illustrates a seasonal (Figure 2a) and day-to-day (Figure 2b) variability of CO_2 and CH_4 at the constant altitude of 40 m AGL in the location close to the city centre. The lowest monthly mole fraction of CO_2 and CH_4 was measured in May and the highest in October. An annual amplitude calculated based on monthly mean values was equal to 25 ppm and 120 ppb for CO_2 and CH_4 respectively. The locations of minimum and maximum values are determined by two factors: (i) the seasonal variability of source/sink activity; and (ii) the intensity of mixing processes occurring in the UBL. A larger day-to-day change observed on the daily means recorded during the cold season is the result of the higher intensity of emission sources in this season and the significant influence of the synoptic situation on the daily mean values.

Systematic measurements of CO_2 and CH_4 vertical profiles (Figure 3) allowed to study their variability on different timescales in an urban environment of Krakow. Distinct seasonal and diurnal variability is observed when data is grouped accordingly: by seasons (colours) and time of the day (panel columns). CO_2 mole fraction varied with altitude depending on time of day. During the day, turbulent mixing of air within the boundary layer averaged the mole fraction within the profile, and CO_2 emissions from anthropogenic and biogenic sources in the area were mitigated by the photosynthesis sink. During the night, diminishing of photosynthesis caused the increase of the net CO_2 flux from the surface, and as a result, together with stable boundary layer (SBL) formation, accumulation of CO_2 near the surface was observed. At the same time, CO_2 mole fraction within the higher part of the profile remained constant regardless of the time of day. The most distinct diurnal variation of the CO_2 profile occurred during the warm season, when biosphere was most active; the highest observed difference between the surface and the free atmosphere of around 150 ppm was observed in autumn. In winter, CO_2 vertical profile varied less, with a minimum observed vertical gradient of 50 ppm. In this season, CO_2 net flux from the biosphere, which is a main driver

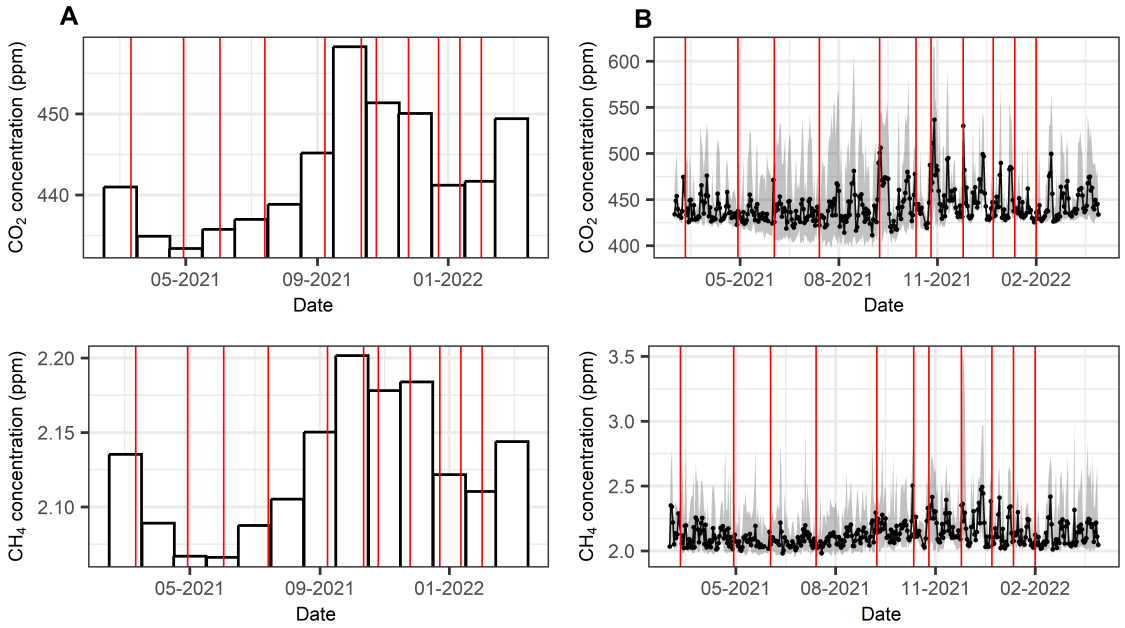

Figure 2. Monthly (A) and daily (B) mean of CO_2 and CH_4 mole fraction from AGH site at 40 m AGL measured using a Picarro G-2311-f analyser for the period from March 2021 to April 2022. The dates of vertical profile measurement campaigns are marked by vertical red lines.

of diurnal variability of surface emissions, is drastically diminished, so the near-surface CO_2 mole fraction remains influenced mainly by the boundary layer diurnal dynamics. CH_4 diurnal variation was most pronounced in the warm season as well, with the highest observed mole fraction difference between the surface and free atmosphere of around 1.2 ppm occurred during summer night (yellow lines in lower panel of Figure 3). The lowest vertical CH_4 gradient within the SBL of 0.3 ppm was observed in winter, indicating temperature-dependent methane sources as main drivers of its mole fraction in the surface layer. Similarly to CO_2, BL diurnal dynamics influenced the vertical profiles of methane.

A detailed BL dynamics description is included in the following sections. A full overview of the data collected in the scope of this study, grouped by campaign and augmented with meteorological data from the AGH site, is available in the Supplement (Figures S5-S26).

3.2 Atmospheric boundary layer dynamics

3.2.1 Transition from convective boundary layer (CBL) to stable boundary layer (SBL)

Measurements collected during the vertical profiling of UBL confirmed the key influence of UBL dynamics on the vertical profiles of CO_2 and CH_4 molar fractions. The evolution of the convective boundary layer and the development of a stable boundary layer is presented in Figure 4 based on results from campaign No. 3. The Campaign was carried out from 1.06.2021

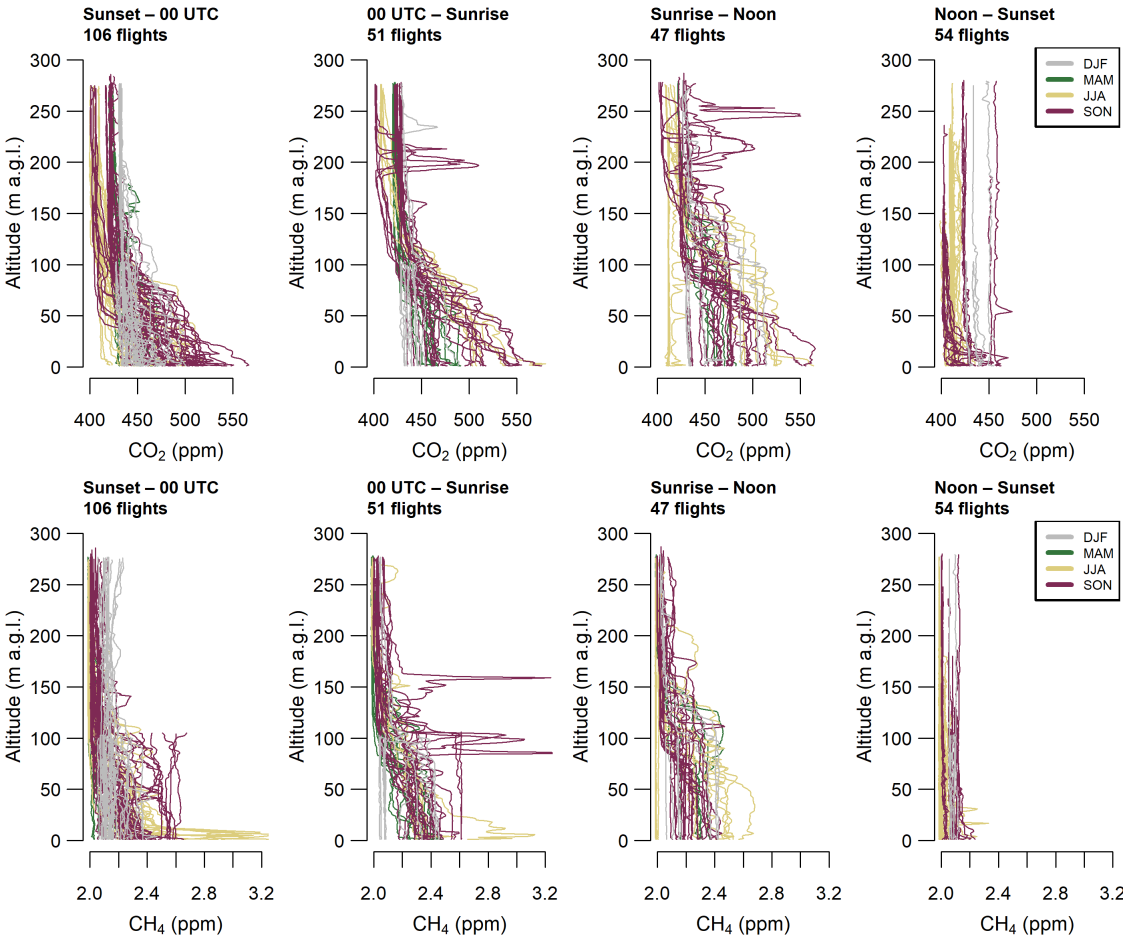

Figure 3. CO_2 and CH_4 vertical profiles divided by season (different colours) and time of day (different columns).

8 UTC until 2.06.2021 5 UTC (44 vertical profiles). Because the daytime flights were performed every 10 minutes, to maintain the readability of Figure 4, only the selected profiles representing one-hour intervals were presented (21 vertical profiles). During the daytime, strong vertical mixing resulted in a constant mole fraction of GHGs in the vertical profile. Between 9 and 16 UTC, the GHG mole fractions in the vertical profile ranged between 408 and 415 ppm for CO_2 and between 1.98 and 2.01 ppm for CH_4, respectively. After 18 UTC CO_2 and CH_4 molar fraction increase was observed close to the ground level. During the night time, a positive temperature gradient (Figure 4) and weak wind speed (less than 3 $\mathrm{m\,s^{-1}}$ - Figure 4) up to 100 m AGL was observed, indicating the formation of an inversion layer. The vertical CO_2 and CH_4 profiles during this period were characterised by an approximately linear decrease in mole fraction up to an altitude of 150 m AGL

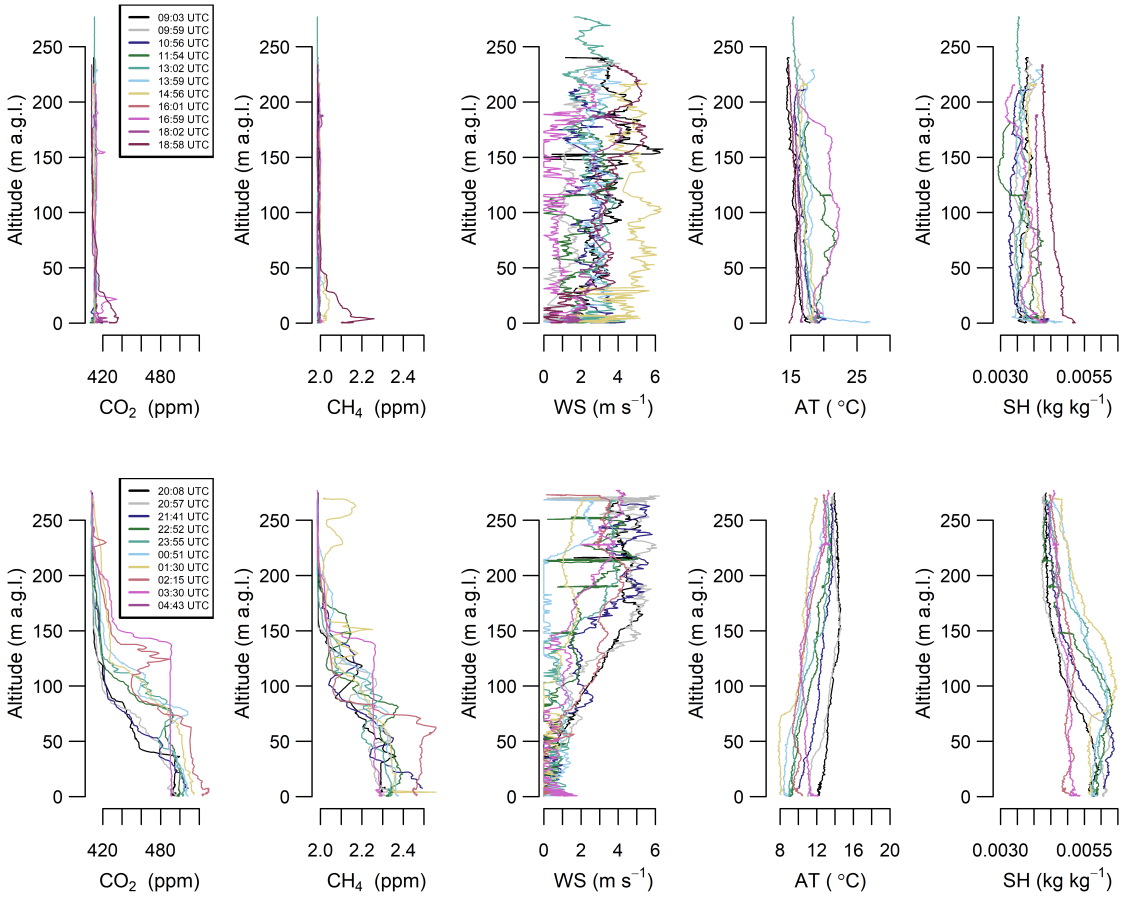

Figure 4. Selected vertical profiles of a) CO_2 and b) CH_4 mole fraction, c) wind speed, d) air temperature and e) specific humidity for campaign No. 3 (01-02.06.2021).

3.2.2 Transition from stable boundary layer (SBL) to convective boundary layer (CBL)

An example of the evolution from a stable boundary layer through the development of the convective layer occurring in the morning hours is presented using data from campaign no. 7 (26.10.2021; flights 20-28; Figure 5). The atmospheric temperature, CO_2 and CH_4 vertical profiles show that over 4 hours between 5:13 UTC and 09:22 UTC the near-ground temperature inversion (of approximately 7 K initially), clearly visible in the first 100 m of the atmosphere, is gradually erased as the increasing surface temperature causes turbulence and mixing, evolving into a well-mixed lower atmosphere when surface temperatures exceed 10 °C. Initially night-time atmosphere is clearly structured, with high variations of CO_2 and CH_4 visible up to 150 m AGL and a distinct elevated CO_2 plumes high aloft (above 200 m AGL). These high and vertically localized gradients, together with an elevated and gently varying specific humidity above 100 m AGL point to a strong shear of plumes emitted upwind into

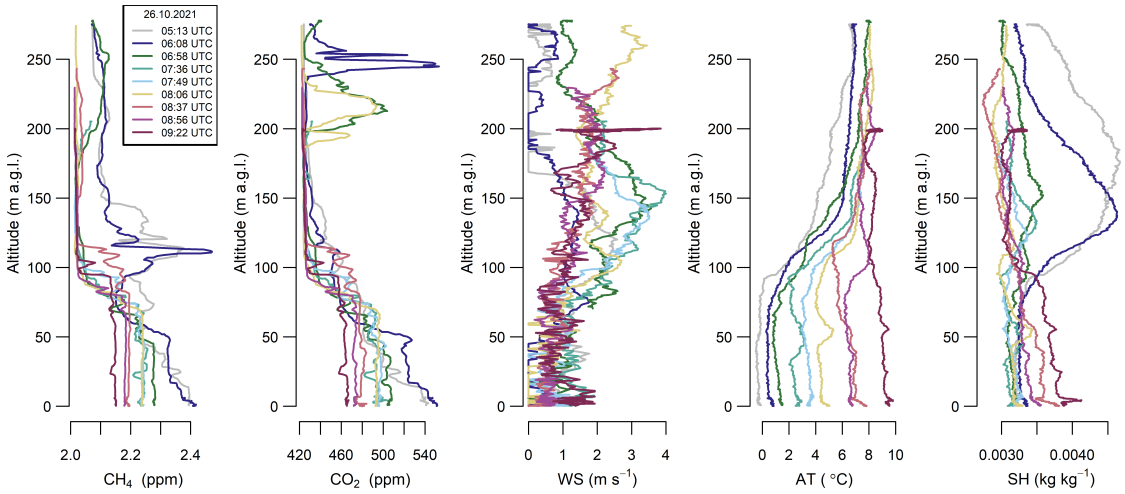

Figure 5. Selected vertical profiles of CH_4 and CO_2 mole fraction, wind speed, air temperature, and H_2O mole fraction measured during sampling campaign no. 7 (26.10.2021).

a residual layer formed on a previous day, transported by varying horizontal winds, strongest at 120 m AGL at 05:13 UTC, and reaching a maximum of 4 $m\,s^{-1}$ at 150 m AGL. Over the morning, the enhancement in GHG mole fractions develops a well-mixed layer that rises together with the inversion cap, crossing 50 m AGL between 07:36 UTC and 07:49 UTC, and reaching approximately 100 m AGL at 09:22 UTC, after which it continues to rise quickly, and is identifiable at 180 m AGL at 09:48 UTC, last flight of the campaign (Figure S17).

3.3 Anomalies in vertical distribution of GHGs - CO_2 case study

Figure 6 presents results from two measurement campaigns for which a plume of CO_2 was visible at an altitude of 200 m AGL (measurements from 8 September 2021) and 200-250 m AGL (measurements from 26 October 2021).

Strong maxima of CO_2 mole fractions observed in the vertical profiles measured on 8 September between 01:00 UTC and 06:20 UTC at approximately 200 m AGL are clearly of different origin than gradually increasing signals closer to the surface (Figure 6a). Such relatively thin nighttime layers with strong enhancements of CO_2 are often generated by CO_2 tall stack emissions typically associated with power generation or industrial activities located upwind of the measurement point. Due to the weak vertical transport in a stable nighttime atmosphere, such plumes can be transported for long distances.

Based on the prevalent wind conditions on the measurement day, as well as available knowledge on the location of the power plants in the vicinity of Krakow, we hypothesise that the observed signal originates from one of the two nearby co-generation plants (Pol. "elektrociepłownia", EC), each powered by hard coal combustion. Those were EC Skawina and EC Krakow (Figure 1). As the available measurements of wind speed and direction were sparse and variable in time and the wind patterns are often complex in the urban environment, it was not possible to identify the source responsible for observed CO_2 enhancements based

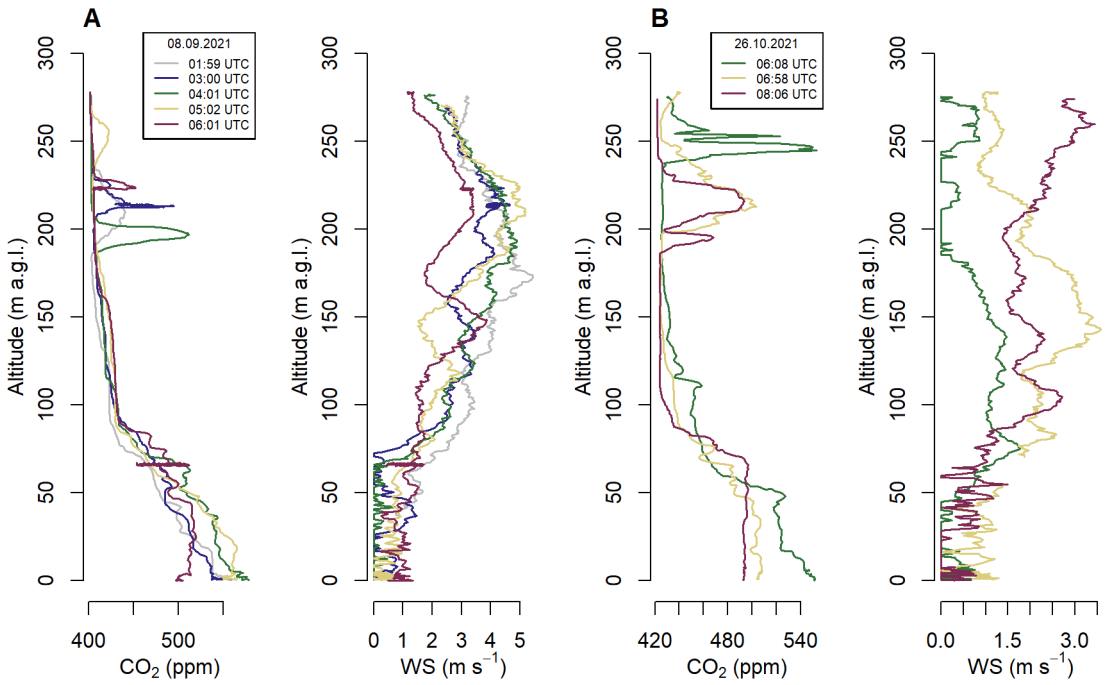

Figure 6. Vertical profiles of CO_2 and wind speed for specific hours at: a) campaign No. 5 (flights 26–30; date: 08.09.2021) and b) campaign No. 7 (flights 21, 22, 25; date: 26.10.2021). On both nights a plume of CO_2 was observed aloft, between 200–250 m AGL

on meteorological parameters only. To overcome this issue WRF-GHG model (Section 2.4) was applied to calculate the CO_2 plume dispersion from the power plants in the times of interest.

WRF model results were verified against meteorological data from the AGH site (Figure S4). The numerical results of wind, air temperature and specific humidity are consistent with the observations. During the night between 7 and 8 September, the model slightly overestimated the air temperature, with a maximum difference of 3°C at 3 UTC 8 September 2021. During the night hours, the model wind speed was overestimated slightly, with observed values between 18 UTC and 6 UTC close to 0.5 $\mathrm{m\,s^{-1}}$ and modelled was equal to 1 $\mathrm{m\,s^{-1}}$.

Numerical results of simulated tagged tracers (see section 2.4) indicated that on the night between 7 and 8 September 2021, between 22 UTC and 6 UTC in the morning, the plume from EC Skawina was advected to the north-east, almost directly along the straight line between the emitting stack of that power plant and the measurement site (Figure 7, left panel). Conversely, the emissions from EC Krakow were advected away from the measurement site, thus the possibility of that installation being a source of the observed plume was excluded (not shown).

An attempt of a direct comparison between simulated and observed vertical distribution of CO_2 was made. However, due to challenges in atmosphere representation of the nighttime stable conditions, the model results are characterised by large spatial variability, with the pointwise and momentary differences between mole fraction enhancements at the measurement location and observation-based enhancements over free tropospheric values varying from 0 ppm to almost 100 ppm at 5:30 UTC (not

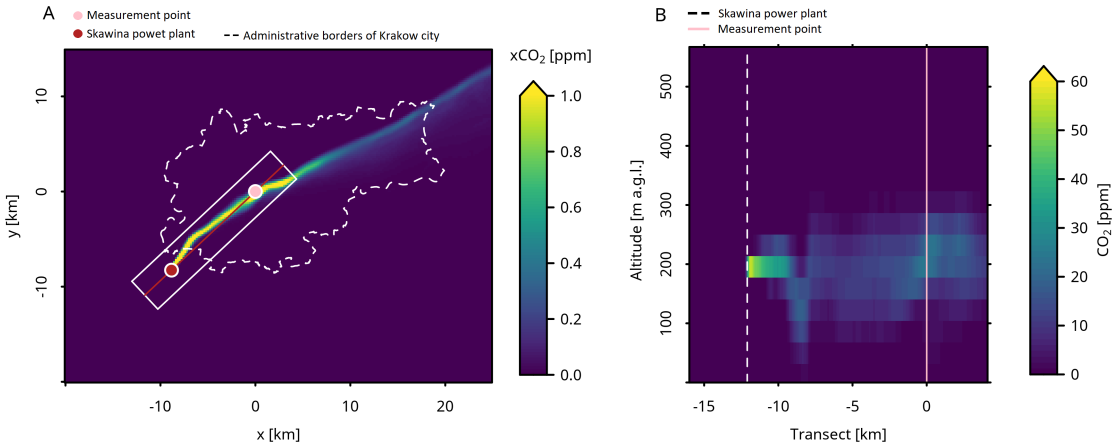

Figure 7. Model-predicted plume mole fraction from EC Skawina power plant at 5:30 UTC 8 September 2021. Panel A: Vertically integrated partial column CO_2 mole fraction (xCO_2). Red: Skawina power plant. Pink: Baloon Site. Panel B: Cross section of CO_2 mole fractions, averaged along the red line over the area marked by the white rectangle in panel A.

shown). These differences can be attributed to inaccuracies in the simulated wind field and vertical mixing of the tracer. To provide a more robust picture, CO_2 modelled mole fractions have been vertically integrated for that time over the city area (Figure 7, left panel), to confirm that the plume was indeed advected from EC Skawina towards the balloon site. Furthermore, by averaging along the cross-section marked with the white rectangle containing the bulk of the emitted plume mass, we can also show that the model predicts that the CO_2 remains elevated at approximately 200 m AGL near the balloon measurement location, similar to where it was measured by the balloon-mounted instrument (Figure 6a). Based on these results it can be concluded that the observed plume originated from the EC Skawina.

3.4 Anomalies in greenhouse gas vertical distribution - CH_4 case study

Similar peaks above the inversion layer have been also observed in the case of CH_4 mole fraction (Figure 8), however, the time of detected plumes and their altitude differs from CO_2. It suggests that in the case of methane, we were also able to detect the plumes emitted from a point source, but the origin and temporal dynamics of this source are different from CO_2. Due to the lack of evident possible source locations, it was not possible to attribute the specific plumes to particular locations using a similar model approach. While the most likely source of emissions are leaks in the city gas network, identification of emission sources requires further studies using model simulations with more realistic methane emission fields for the city.

4 Conclusions

The measurement report describes 12 monthly-based UBL profiling measurement campaigns conducted between March 2021 and February 2022 in the city of Krakow (Southern Poland). The measurements incorporated the basic meteorological pa-

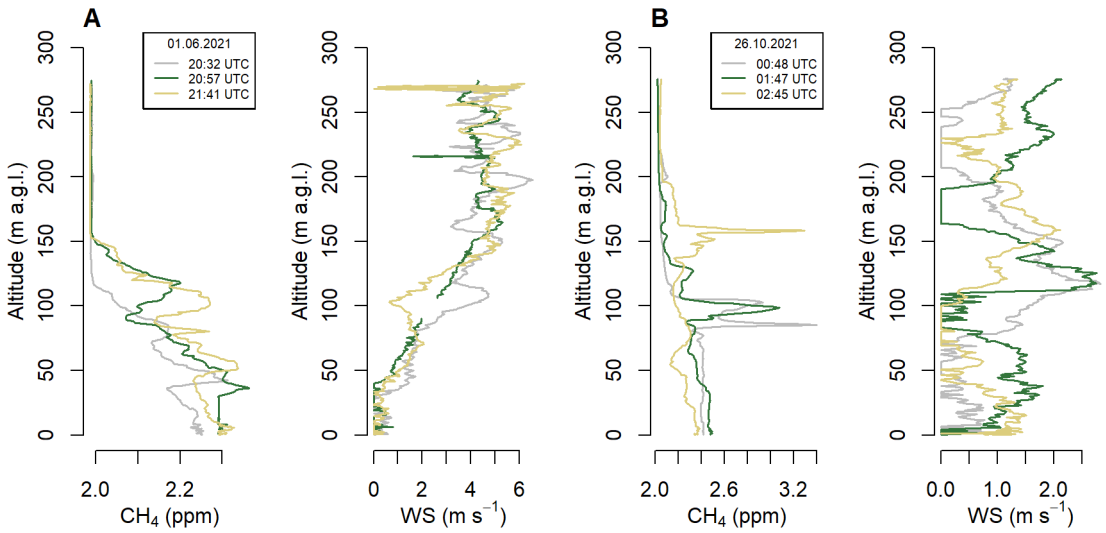

Figure 8. Vertical profiles of CH_4 and wind speed for specific hours at a) campaign 3 (flights 39-41; 01.06.2021) and b) campaign 7 (flights 15-17; 26.10.2021), when Gaussian plumes of CH_4 were observed.

rameters (temperature, relative humidity, pressure, wind speed) and CO_2 and CH_4 molar fractions recorded with 1 s temporal resolution along the profiles ranging from ground level up to 280 m AGL. During each campaign several profiles were collected with at least hourly resolution covering all periods of the day, mainly focused on the formation, development and decaying of the inversion layer within UBL. Surprisingly, as unplanned added value, a CO_2 and CH_4 plumes occurring above the inversion layer were observed in selected profiles. The presented dataset contributes to a better understanding of the boundary layer dynamics over urban areas. Despite the limitation that the dataset contains the observations from a specific location, its analysis can be expanded for other cities located within similar concave terrain, providing an opportunity to verify different tools aiming at estimating urban carbon emissions. The additional signals representing plumes from industrial point sources allowed validation of the performance of the high-resolution numerical atmospheric transport model and enabled the identification of the source location. Moreover, the identification of CH_4 signals in UBL indicates the potential for reporting unexpected methane emissions. Identifying the specific sources proved to require more sophisticated data on the spatial emission distribution. From the methodological point of view, carrying out profile measurements requires instruments capable of fast and precise detection of changes in measured parameters (both GHG mole fractions and meteorological variables) which can change rapidly with height. The response time of temperature sensors turned out to be crucial when measuring vertical gradients, indicating the advantage of less inert thermocouple sensors compared to semiconductor sensors. In the case of measuring the wind direction, it turned out that despite corrections using an accelerometer and magnetometer, interference related to the disturbance of the magnetic field by powering the drone's engines, or uncontrolled sudden rotational and lateral movements of the tethered balloon during descent caused the measurement being unreliable. Hence, other solutions for this parameter measurement are recommended than the one used here.

Code and data availability. ERA5 data available via Copernicus Climate Data Store (CDS; Hersbach et al., 2017). The measurements data set is available for download from the ICOS Carbon Portal (https://doi.org/10.18160/8DSK-R4JS; Zimnoch et al., 2023).

Author contributions. MZ, MG conceptualised and prepared the study, and also drafted and finalised the manuscript. MZ, MG, PS, AJK, ŁC processed, analysed and visualised the presented data. MG and PS provided WRF-GHG model runs and analysis. All co-authors contributed to the carrying out of the measurement campaigns as well as manuscript preparation.

Competing interests. The authors declare that they have no conflict of interest.

Acknowledgements. This project has been partially supported by the European Union's Horizon 2020 research and innovation programme under grant agreements No. 958927 and No. 101037319, and the subsidy of the Ministry of Education and Science. The research results presented in this paper have been developed with the use of equipment financed from the funds of the "Excellence Initiative - Research University" program at AGH University of Krakow. We gratefully acknowledge Polish high-performance computing infrastructure PLGrid (HPC Centers: ACK Cyfronet AGH) for providing computer facilities and support within computational grants no. PLG/2021/014946, PLG/2022/015860, PLG/2023/016669 and the "Balon Widokowy sp. z o.o." crew members for providing the balloon platform for the experiments and support during the campaigns.

References

Ashworth, K., Bucci, S., Gallimore, P. J., Lee, J., Nelson, B. S., Sanchez-Marroquín, A., Schimpf, M. B., Smith, P. D., Drysdale, W. S., Hopkins, J. R., Lee, J. D., Pitt, J. R., Di Carlo, P., Krejci, R., and McQuaid, J. B.: Megacity and local contributions to regional air pollution: an aircraft case study over London, Atmospheric Chemistry and Physics, 20, 7193–7216, https://doi.org/10.5194/acp-20-7193-2020, 2020.

Ballabio, C., Panagos, P., and Monatanarella, L.: Mapping topsoil physical properties at European scale using the LUCAS database, Geoderma, 261, 110–123, https://doi.org/https://doi.org/10.1016/j.geoderma.2015.07.006, 2016.

Beck, V., Gerbig, C., Koch, T., Bela, M. M., Longo, K. M., Freitas, S. R., Kaplan, J. O., Prigent, C., Bergamaschi, P., and Heimann, M.: WRF-Chem simulations in the Amazon region during wet and dry season transitions: evaluation of methane models and wetland inundation maps, Atmospheric Chemistry and Physics, 13, 7961–7982, https://doi.org/10.5194/acp-13-7961-2013, 2013.

Bezyk, Y., Górka, M., Sówka, I., Nęcki, J., and Strąpoć, D.: Temporal dynamics and controlling factors of CO2 and CH4 variability in the urban atmosphere of Wroclaw, Poland, Science of The Total Environment, 893, 164 771, https://doi.org/https://doi.org/10.1016/j.scitotenv.2023.164771, 2023.

Brunner, D., Kuhlmann, G., Henne, S., Koene, E., Kern, B., Wolff, S., Voigt, C., Jöckel, P., Kiemle, C., Roiger, A., Fiehn, A., Krautwurst, S., Gerilowski, K., Bovensmann, H., Borchardt, J., Galkowski, M., Gerbig, C., Marshall, J., Klonecki, A., Prunet, P., Hanfland, R., Pattantyús-Ábrahám, M., Wyszogrodzki, A., and Fix, A.: Evaluation of simulated CO_2 power plant plumes from six high-resolution atmospheric transport models, Atmospheric Chemistry and Physics, 23, 2699–2728, https://doi.org/10.5194/acp-23-2699-2023, 2023.

CLC: CORINE Land Cover (CLC) inventory for 2018, v20u1, database, last access: June 2nd, 2023, land.copernicus.eu/pan-european/corine-land-cover/clc2018, 2020.

Crawford, B., Christen, A., and McKendry, I.: Diurnal Course of Carbon Dioxide Mixing Ratios in the Urban Boundary Layer in Response to Surface Emissions, Journal of Applied Meteorology and Climatology, 55, 507 – 529, https://doi.org/10.1175/JAMC-D-15-0060.1, 2016.

Dietrich, F., Chen, J., Voggenreiter, B., Aigner, P., Nachtigall, N., and Reger, B.: MUCCnet: Munich Urban Carbon Column network, Atmospheric Measurement Techniques, 14, 1111–1126, https://doi.org/10.5194/amt-14-1111-2021, 2021.

Duren, R. M. and Miller, C. E.: Measuring the carbon emissions of megacities, Nature Climate Change, 2, 560–562, https://doi.org/10.1038/nclimate1629, 2012.

Dy, C. Y. and Fung, J. C. H.: Updated global soil map for the Weather Research and Forecasting model and soil moisture initialization for the Noah land surface model, Journal of Geophysical Research: Atmospheres, 121, 8777–8800, https://doi.org/https://doi.org/10.1002/2015JD024558, 2016.

EEA: Industrial Reporting under the Industrial Emissions Directive 2010/75/EU and European Pollutant Release and Transfer Register Regulation (EC) No 166/2006 - ver. 10.0 Dec 2023 (Tabular data), https://doi.org/10.2909/63a14e09-d1f5-490d-80cf-6921e4e69551, 2023.

ESA: Copernicus DEM - Global and European Digital Elevation Model (COP-DEM), Database, https://doi.org/10.5270/ESA-c5d3d65, 2022.

ESDAC: European Soild Data Centre - Topsoil physical properties for Europe data, website, last access: June 2nd, 2023, https://esdac.jrc.ec.europa.eu/content/topsoil-physical-properties-europe-based-lucas-topsoil-data, 2023.

Fiehn, A., Kostinek, J., Eckl, M., Klausner, T., Gałkowski, M., Chen, J., Gerbig, C., Röckmann, T., Maazallahi, H., Schmidt, M., Korbeń, P., Nęçki, J., Jagoda, P., Wildmann, N., Mallaun, C., Bun, R., Nickl, A.-L., Jöckel, P., Fix, A., and Roiger, A.: Estimating CH_4, CO_2 and

CO emissions from coal mining and industrial activities in the Upper Silesian Coal Basin using an aircraft-based mass balance approach, Atmospheric Chemistry and Physics, 20, 12 675–12 695, https://doi.org/10.5194/acp-20-12675-2020, 2020.

Gałkowski, M., Jordan, A., Rothe, M., Marshall, J., Koch, F.-T., Chen, J., Agusti-Panareda, A., Fix, A., and Gerbig, C.: In situ observations of greenhouse gases over Europe during the CoMet 1.0 campaign aboard the HALO aircraft, Atmospheric Measurement Techniques, 14, 1525–1544, https://doi.org/10.5194/amt-14-1525-2021, 2021.

Giovannini, L., Ferrero, E., Karl, T., Rotach, M. W., Staquet, C., Trini Castelli, S., and Zardi, D.: Atmospheric Pollutant Dispersion over Complex Terrain: Challenges and Needs for Improving Air Quality Measurements and Modeling, Atmosphere, 11, https://doi.org/10.3390/atmos11060646, 2020.

Grell, G. A., Peckham, S. E., Schmitz, R., McKeen, S. A., Frost, G., Skamarock, W. C., and Eder, B.: Fully coupled "online" chemistry within the WRF model, Atmospheric Environment, 39, 6957–6975, https://doi.org/https://doi.org/10.1016/j.atmosenv.2005.04.027, 2005.

Hedworth, H., Page, J., Sohl, J., and Saad, T.: Investigating Errors Observed during UAV-Based Vertical Measurements Using Computational Fluid Dynamics, Drones, 6, https://doi.org/10.3390/drones6090253, 2022.

Hersbach, H., Bell, B., Berrisford, P., Hirahara, S., Horányi, A., Muñoz-Sabater, J., Nicolas, J., Peubey, C., Radu, R., Schepers, D., Simmons, A., Soci, C., Abdalla, S., Abellan, X., Balsamo, G., Bechtold, P., Biavati, G., Bidlot, J., Bonavita, M., De Chiara, G., Dahlgren, P., Dee, D., Diamantakis, M., Dragani, R., Flemming, J., Forbes, R., Fuentes, M., Geer, A., Haimberger, L., Healy, S., Hogan, R. J., Hólm, E., Janisková, M., Keeley, S., Laloyaux, P., Lopez, P., Lupu, C., Radnoti, G., de Rosnay, P., Rozum, I., Vamborg, F., Villaume, S., and Thépaut, J.-N.: Complete ERA5 global atmospheric reanalysis, Dataset, https://doi.org/10.24381/cds.143582cf, 2017.

IMGW-PIB: IMGW-PIB Forecast Website, website, last access: June 2nd, 2023, meteo.imgw.pl, 2023.

IPCC: Climate Change 2021: The Physical Science Basis. Contribution of Working Group I to the Sixth Assessment Report of the Intergovernmental Panel on Climate Change, vol. In Press, Cambridge University Press, Cambridge, United Kingdom and New York, NY, USA, https://doi.org/10.1017/9781009157896, 2021.

Jasek-Kamińska, A., Zimnoch, M., Wachniew, P., and Różański, K.: Urban CO2 Budget: Spatial and Seasonal Variability of CO2 Emissions in Krakow, Poland, Atmosphere, 11, https://doi.org/10.3390/atmos11060629, 2020.

Keppel-Aleks, G., Wennberg, P. O., and Schneider, T.: Sources of variations in total column carbon dioxide, Atmospheric Chemistry and Physics, 11, 3581–3593, https://doi.org/10.5194/acp-11-3581-2011, 2011.

Kunz, M., Lavric, J. V., Gerbig, C., Tans, P., Neff, D., Hummelgård, C., Martin, H., Rödjegård, H., Wrenger, B., and Heimann, M.: COCAP: a carbon dioxide analyser for small unmanned aircraft systems, Atmospheric Measurement Techniques, 11, 1833–1849, https://doi.org/10.5194/amt-11-1833-2018, 2018.

Lampert, A., Pätzold, F., Asmussen, M. O., Lobitz, L., Krüger, T., Rausch, T., Sachs, T., Wille, C., Sotomayor Zakharov, D., Gaus, D., Bansmer, S., and Damm, E.: Studying boundary layer methane isotopy and vertical mixing processes at a rewetted peatland site using an unmanned aircraft system, Atmospheric Measurement Techniques, 13, 1937–1952, https://doi.org/10.5194/amt-13-1937-2020, 2020.

Li, Y., Deng, J., Mu, C., Xing, Z., and Du, K.: Vertical distribution of CO2 in the atmospheric boundary layer: Characteristics and impact of meteorological variables, Atmospheric Environment, 91, 110–117, https://doi.org/https://doi.org/10.1016/j.atmosenv.2014.03.067, 2014.

Lopez-Coto, I., Hicks, M., Karion, A., Sakai, R. K., Demoz, B., Prasad, K., and Whetstone, J.: Assessment of Planetary Boundary Layer Parameterizations and Urban Heat Island Comparison: Impacts and Implications for Tracer Transport, Journal of Applied Meteorology and Climatology, 59, 1637 – 1653, https://doi.org/10.1175/JAMC-D-19-0168.1, 2020.

McKinney, K. A., Wang, D., Ye, J., de Fouchier, J.-B., Guimarães, P. C., Batista, C. E., Souza, R. A. F., Alves, E. G., Gu, D., Guenther, A. B., and Martin, S. T.: A sampler for atmospheric volatile organic compounds by copter unmanned aerial vehicles, Atmospheric Measurement Techniques, 12, 3123–3135, https://doi.org/10.5194/amt-12-3123-2019, 2019.

NIES: GOSAT-2, website, last access: June 2nd, 2023, www.gosat-2.nies.go.jp, 2023.

NOAA: Trends in Atmospheric Carbon Dioxide, web press release, last access: 15 May 2024, https://www.noaa.gov/news-release/greenhouse-gases-continued-to-increase-rapidly-in-2022, 2024.

Ou, Y., Roney, C., Alsalam, J., Calvin, K., Creason, J., Edmonds, J., Fawcett, A. A., Kyle, P., Narayan, K., O'Rourke, P., Patel, P., Ragnauth, S., Smith, S. J., and McJeon, H.: Deep mitigation of CO2 and non-CO2 greenhouse gases toward 1.5 °C and 2 °C futures, Nature Communications, 12, 6245, https://doi.org/10.1038/s41467-021-26509-z, 2021.

Park, M.-S., Park, S.-H., Chae, J.-H., Choi, M.-H., Song, Y., Kang, M., and Roh, J.-W.: High-resolution urban observation network for user-specific meteorological information service in the Seoul Metropolitan Area, South Korea, Atmospheric Measurement Techniques, 10, 1575–1594, https://doi.org/10.5194/amt-10-1575-2017, 2017.

Peng, Y., Hu, C., Ai, X., Li, Y., Gao, L., Liu, H., Zhang, J., and Xiao, W.: Improvements of Simulating Urban Atmospheric CO2 Concentration by Coupling with Emission Height and Dynamic Boundary Layer Variations in WRF-STILT Model, Atmosphere, 14, https://doi.org/10.3390/atmos14020223, 2023.

Reum, F., Gerbig, C., Lavric, J. V., Rella, C. W., and Göckede, M.: Correcting atmospheric CO_2 and CH_4 mole fractions obtained with Picarro analyzers for sensitivity of cavity pressure to water vapor, Atmospheric Measurement Techniques, 12, 1013–1027, https://doi.org/10.5194/amt-12-1013-2019, 2019.

Richardson, S. J., Miles, N. L., Davis, K. J., Lauvaux, T., Martins, D. K., Turnbull, J. C., McKain, K., Sweeney, C., and Cambaliza, M. O. L.: Tower measurement network of in-situ CO2, CH4, and CO in support of the Indianapolis FLUX (INFLUX) Experiment, Elementa: Science of the Anthropocene, 5, https://doi.org/10.1525/elementa.140, 59, 2017.

Sekuła, P., Bokwa, A., Bartyzel, J., Bochenek, B., Chmura, Ł., Gałkowski, M., and Zimnoch, M.: Measurement report: Effect of wind shear on PM_{10} concentration vertical structure in the urban boundary layer in a complex terrain, Atmospheric Chemistry and Physics, 21, 12 113–12 139, https://doi.org/10.5194/acp-21-12113-2021, 2021a.

Sekuła, P., Bokwa, A., Ustrnul, Z., Zimnoch, M., and Bochenek, B.: The impact of a foehn wind on PM10 concentrations and the urban boundary layer in complex terrain: a case study from Kraków, Poland, Tellus B: Chemical and Physical Meteorology, https://doi.org/10.1080/16000889.2021.1933780, 2021b.

Sekuła, P., Zimnoch, M., Bartyzel, J., Bokwa, A., Kud, M., and Necki, J.: Ultra-Light Airborne Measurement System for Investigation of Urban Boundary Layer Dynamics., Sensors (Basel), 21, https://doi.org/10.3390/s21092920, 2021c.

Siewert, J. and Kroszczynski, K.: GIS Data as a Valuable Source of Information for Increasing Resolution of the WRF Model for Warsaw, Remote Sensing, 12, https://doi.org/10.3390/rs12111881, 2020.

Skamarock, W. C., Klemp, J. B., Dudhia, J., Gill, D. O., Barker, D., Duda, M. G., Xiang-yu, H., Wei, W., and Powers, J. G.: A Description of the Advanced Research WRF Version 3 (No. NCAR/TN-475+STR), Tech. rep., University Corporation for Atmospheric Research, 2008.

TCCON: TCCON, website, last access: June 2nd, 2023, http://www.tccon.caltech.edu/, 2023.

Thilakan, V., Pillai, D., Gerbig, C., Galkowski, M., Ravi, A., and Anna Mathew, T.: Towards monitoring the CO_2 source–sink distribution over India via inverse modelling: quantifying the fine-scale spatiotemporal variability in the atmospheric CO_2 mole fraction, Atmospheric Chemistry and Physics, 22, 15 287–15 312, https://doi.org/10.5194/acp-22-15287-2022, 2022.

Tong, X., van Heuven, S., Scheeren, B., Kers, B., Hutjes, R., and Chen, H.: Aircraft-Based AirCore Sampling for Estimates of N₂O and CH₄ Emissions, ENVIRONMENTAL SCIENCE & TECHNOLOGY, 57, 15 571–15 579, https://doi.org/10.1021/acs.est.3c04932, 2023.

Turnbull, J. C., Karion, A., Fischer, M. L., Faloona, I., Guilderson, T., Lehman, S. J., Miller, B. R., Miller, J. B., Montzka, S., Sherwood, T., Saripalli, S., Sweeney, C., and Tans, P. P.: Assessment of fossil fuel carbon dioxide and other anthropogenic trace gas emissions from airborne measurements over Sacramento, California in spring 2009, Atmospheric Chemistry and Physics, 11, 705–721, https://doi.org/10.5194/acp-11-705-2011, 2011.

USK: Urząd Statystyczny w Krakowie, website, last access: June 2nd, 2023, https://krakow.stat.gov.pl/, 2023.

van der Woude, A. M., de Kok, R., Smith, N., Luijkx, I. T., Botía, S., Karstens, U., Kooijmans, L. M. J., Koren, G., Meijer, H. A. J., Steeneveld, G.-J., Storm, I., Super, I., Scheeren, H. A., Vermeulen, A., and Peters, W.: Near-real-time CO_2 fluxes from CarbonTracker Europe for high-resolution atmospheric modeling, Earth System Science Data, 15, 579–605, https://doi.org/10.5194/essd-15-579-2023, 2023.

Veefkind, J., Aben, I., McMullan, K., Förster, H., de Vries, J., Otter, G., Claas, J., Eskes, H., de Haan, J., Kleipool, Q., van Weele, M., Hasekamp, O., Hoogeveen, R., Landgraf, J., Snel, R., Tol, P., Ingmann, P., Voors, R., Kruizinga, B., Vink, R., Visser, H., and Levelt, P.: TROPOMI on the ESA Sentinel-5 Precursor: A GMES mission for global observations of the atmospheric composition for climate, air quality and ozone layer applications, Remote Sensing of Environment, 120, 70–83, https://doi.org/https://doi.org/10.1016/j.rse.2011.09.027, the Sentinel Missions - New Opportunities for Science, 2012.

Wei, C., Wang, M., Fu, Q., Dai, C., Huang, R., and Bao, Q.: Temporal characteristics of greenhouse gases (CO2 and CH4) in the megacity Shanghai, China: Association with air pollutants and meteorological conditions, Atmospheric Research, 235, 104 759, https://doi.org/https://doi.org/10.1016/j.atmosres.2019.104759, 2020.

Zhang, L., Davis, K. J., Schuh, A. E., Jacobson, A. R., Pal, S., Cui, Y. Y., Baker, D., Crowell, S., Chevallier, F., Remaud, M., Liu, J., Weir, B., Philip, S., Johnson, M. S., Deng, F., and Basu, S.: Multi-Season Evaluation of CO2 Weather in OCO-2 MIP Models, Journal of Geophysical Research: Atmospheres, 127, e2021JD035 457, https://doi.org/https://doi.org/10.1029/2021JD035457, e2021JD035457 2021JD035457, 2022.

Zimnoch, M., Necki, J., Chmura, L., Jasek, A., Jelen, D., Galkowski, M., Kuc, T., Gorczyca, Z., Bartyzel, J., and Rozanski, K.: Quantification of carbon dioxide and methane emissions in urban areas: source apportionment based on atmospheric observations, Mitigation and Adaptation Strategies for Global Change, 24, 1051–1071, https://doi.org/10.1007/s11027-018-9821-0, 2019.

Zimnoch, M., Sekula, P., Jasek-Kaminska, A., Skiba, A., Gałkowski, M., Chmura, L., Bartyzel, J., Jagoda, P., Kud, M., and Necki, J.: Observational datasets of urban CO2 fluxes, atmospheric vertical profiles of CO2 and CH4 and 14CO2, and isotopic composition of atmospheric CO2 at Krakow, Poland; period 2021-2023; part of the CoCO2 project, Dataset, https://doi.org/10.18160/8DSK-R4JS, 2023.